JGR Solid Earth

RESEARCH ARTICLE
10.1029/2024JB029656

The Collaborative Seismic Earth Model: Generation 2

Sebastian Noe[1], **Dirk-Philip van Herwaarden**[1], **Solvi Thrastarson**[1], **Marta Pienkowska**[1], **Neda Masouminia**[1,2,3], **Jincheng Ma**[2,4], **Hans-Peter Bunge**[2], **Deborah Wehner**[5], **Nicholas Rawlinson**[5], **Yajian Gao**[6,7], **Frederik Tilmann**[6], **Artie Rodgers**[8], and **Andreas Fichtner**[1]

[1]Department of Earth and Planetary Sciences, Institute of Geophysics, ETH Zurich, Zurich, Switzerland, [2]Department of Earth and Environmental Sciences, Ludwig-Maximilians-Universität München, Munich, Germany, [3]Department of Seismology, University of Tehran, Tehran, Iran, [4]School of Earth and Space Sciences, Peking University, Beijing, China, [5]Department of Earth Sciences, Bullard Laboratories, University of Cambridge, Cambridge, UK, [6]GFZ German Research Centre for Geosciences, Potsdam, Germany, [7]Karlsruhe Institute of Technology, Karlsruhe, Germany, [8]Lawrence Livermore National Laboratory, Geophysical Monitoring Program, Livermore, CA, USA

Key Points:

- We present a global seismic Earth model that combines regional models through global full-waveform inversion
- The model circumvents crustal corrections by jointly inverting for crustal and mantle structure
- Global waveforms are explained to 50 s period, while regional models retain their shorter-period resolution below 20 s

Supporting Information:

Supporting Information may be found in the online version of this article.

Correspondence to:

S. Noe,
sebastian.noe@eaps.ethz.ch

Citation:

Noe, S., van Herwaarden, D.-P., Thrastarson, S., Pienkowska, M., Masouminia, N., Ma, J., et al. (2024). The Collaborative Seismic Earth Model: Generation 2. *Journal of Geophysical Research: Solid Earth*, *129*, e2024JB029656. https://doi.org/10.1029/2024JB029656

Received 5 JUN 2024
Accepted 27 NOV 2024

Author Contributions:

Conceptualization: Sebastian Noe, Dirk-Philip van Herwaarden, Solvi Thrastarson, Andreas Fichtner
Data curation: Sebastian Noe, Dirk-Philip van Herwaarden, Solvi Thrastarson
Formal analysis: Sebastian Noe
Funding acquisition: Andreas Fichtner
Investigation: Sebastian Noe, Marta Pienkowska
Methodology: Sebastian Noe, Dirk-Philip van Herwaarden, Solvi Thrastarson, Marta Pienkowska, Andreas Fichtner
Project administration: Andreas Fichtner
Resources: Dirk-Philip van Herwaarden, Solvi Thrastarson, Neda Masouminia, Jincheng Ma, Hans-Peter Bunge, Deborah Wehner, Nicholas Rawlinson,

Abstract

Geological interpretations, earthquake source inversions and ground motion modeling, among other applications, require models that jointly resolve crustal and mantle structure. With the second generation of the Collaborative Seismic Earth Model (CSEM2), we present a global multi-resolution tomographic Earth model that serves this purpose. The model evolves through successive regional- and global-scale refinements. While the first generation aggregated regional models, with this study, we ensure consistency between all individual submodels, resulting in a model that accurately explains wave propagation across scales. Recent regional tomographic models were incorporated, comprising continental-scale inversions for Asia and Africa, as well as regional inversions for the Western US, Central Andes, Iran, and Southeast Asia. Across all regional refinements, over 793,000 source-receiver pairs contributed. Moreover, the long-wavelength Earth model (LOWE) introduces large-scale structures outside of pre-existing local refinements. A full-waveform inversion for global anisotropic P-and S-wave speed structure over a total of 194 iterations with a minimum period of 50 s on a large data set of 1 hr of waveform data from 2,423 earthquakes and over 6 million source-receiver pairs ensures that regional updates in the crust and uppermost mantle translate into updates of deeper, global-scale structure. To test the performance of CSEM2, we evaluate waveform fits between observed and synthetic seismograms at 50 s for an independent data set on the global scale, and on the regional scale for lower periods. We accurately simulate waveforms within and across regional refinements, maintaining the original resolution of the submodels embedded in the global framework.

Plain Language Summary

Seismic wave propagation is an important tool to learn more about the Earth's interior structure. Specifically, seismologists create wave speed maps for the crust and mantle called tomographic models that help geologists interpret the dynamics and evolution of the planet. A method to develop tomographic models is through full-waveform inversion (FWI), which relies on physically accurate numerical simulations of the Earth's response to an earthquake. Here, we combine multiple regional-scale tomographic studies developed with FWI into one global model. New regions encompass Africa and Asia on the continental scale, and Iran, the Western US, Southeast Asia, and the Central Andes on the regional scale. Furthermore, we incorporate findings from a global FWI model to add resolution in regions without many earthquakes and seismic stations. The strength of this workflow lies in resolving crustal and mantle structure simultaneously. To ensure consistency within the model, we perform a global FWI on top of the assembled regions. We present depth slices of the final tomographic model (CSEM2) and compare computed and observed seismic data on different regional scales.

1. Introduction

Seismic tomographic models spanning various scales and resolutions have practical applications in numerous research areas. At the global scale, these models provide information to constrain Earth's structure and its evolution (Bott et al., 2024; Bunge et al., 2003; Koelemeijer et al., 2013; Trampert et al., 2004). Locally, tomographic models are an essential component of ground motion modeling that help to assess earthquake impacts (Chaljub et al., 2010; Gallovič et al., 2010; Graves & Pitarka, 2010; Komatitsch et al., 2004; Lomax & Bolt, 1992). Across all scales, three-dimensional wave speed structures enhance earthquake characterizations

Yajian Gao, Frederik Tilmann, Artie Rodgers, Andreas Fichtner
Software: Sebastian Noe, Dirk-Philip van Herwaarden, Solvi Thrastarson
Supervision: Dirk-Philip van Herwaarden, Solvi Thrastarson, Marta Pienkowska, Andreas Fichtner
Validation: Sebastian Noe
Visualization: Sebastian Noe
Writing – original draft: Sebastian Noe, Dirk-Philip van Herwaarden, Solvi Thrastarson, Marta Pienkowska, Neda Masouminia, Jincheng Ma, Hans-Peter Bunge, Deborah Wehner, Nicholas Rawlinson, Yajian Gao, Frederik Tilmann, Artie Rodgers, Andreas Fichtner
Writing – review & editing: Sebastian Noe, Dirk-Philip van Herwaarden, Solvi Thrastarson, Marta Pienkowska, Neda Masouminia, Jincheng Ma, Hans-Peter Bunge, Deborah Wehner, Nicholas Rawlinson, Yajian Gao, Frederik Tilmann, Artie Rodgers, Andreas Fichtner

(Donner et al., 2020; Hjörleifsdóttir & Ekström, 2010; Zhou et al., 2016), thus providing more accurate Green's functions in moment tensor inversions and reducing trade-offs between source parameters (Hejrani et al., 2017; Hingee et al., 2011; Simutė et al., 2023; Wang & Zhan, 2020a, 2020b; L. Zhu & Zhou, 2016). In this study, we present a publicly available, multi-scale seismic tomographic model that effectively bridges the gap between regional and global applications within a single framework.

Our global multi-scale model employs full-waveform inversion (FWI) with gradient computations based on the adjoint-state method, enabling iterative updates from an initial model to gradually minimize the misfit between observed and computed waveforms (Fichtner et al., 2006; Lailly & Bednar, 1983; Liu & Tromp, 2006; Tarantola, 1984). This process requires repeated numerical simulations of seismic waves propagating through the globe subject to the visco-elastic wave equation, leading to a computationally demanding workflow. Many tomographic methods circumvent this limitation by employing either ray-based approaches (e.g., Amaru, 2007; Simmons et al., 2021), or finite-frequency approximations (e.g., Dahlen et al., 2000; Marquering et al., 1999). FWI considers any incoming recorded wave within the imaged Earth model, thereby increasing the volumetric sensitivity for each earthquake measurement (Tromp, 2020). Combined with the emergence of GPU accelerated computations (Rietmann et al., 2012), modern computational capabilities allow us to apply FWI to solve relevant problems in seismic tomography.

Regardless of the method, the quality of the tomographic Earth models depends on the available data. In global seismology, the coverage is strongly heterogeneous since earthquakes primarily occur near tectonic plate boundaries, while seismic stations are mainly located on land. Therefore, the achievable model resolution strongly depends on the region. As a result, the resolution of global tomographic models in well-covered areas is usually held back by the costs of running high-frequency numerical simulations for the entire globe rather than by data availability. Focusing the application of tomography to well-covered areas only without considering remote regions allows the inversion to be primarily data-driven, motivating regional tomographic studies in the first place. The first generation of the Collaborative Seismic Earth Model (CSEM1) (Fichtner et al., 2018) addresses this issue, embedding regional tomographic models into a global context and providing a framework for a comprehensive multi-scale approach that images the crust and the mantle. In this second generation (CSEM2), we not only introduce further regional refinements, but also extend the framework with an overarching global FWI to ensure consistency for seismic wave propagation across scales.

In the following, we explain the parametrization of CSEM2 and its submodels. We highlight the new regional refinements, and we outline the strategy for the global inversion. Finally, we pursue a data-driven approach towards validating the second generation CSEM on global and regional scales.

2. Model Assembly

2.1. Parametrization

A detailed description of the parametrization and construction of the CSEM can be found in Fichtner et al. (2018). In the interest of completeness, we summarize the key aspects.

The CSEM provides a framework to consistently build upon accumulated prior knowledge and to progressively incorporate new information, embedding regional models in the global domain. It is a radially anisotropic visco-anelastic model, described by the elastic parameters, attenuation, and density. However, because waveform sensitivity is mainly focused on isotropic P-wave speed and vertically and horizontally polarized S-wave speeds, anisotropic P-wave speeds and density are only updated in some regional refinements, while attenuation is not refined in the inversions.

Overall, the regional incorporations can be understood as a type of mini-batch updates to the global model, where only a regionally constrained selection of earthquakes contributes to the given update from a submodel. When extracting CSEM2 for a region, all submodels available in that region contribute to the final result with their respective original parametrization. Model values of intersecting submodels are then interpolated in the order in which they have been included onto some spatial discretization defined before the extraction process, for example, a point cloud or a spectral-element mesh. Therefore, CSEM2 is not restricted to a specific grid, but can be extracted in an arbitrary fashion, supporting the multi-scale nature of the model. The wave speed and density values of submodels in the CSEM are defined as the difference with respect to the state of the CSEM prior to the inclusion of that submodel. This enables cosine-tapering of submodels toward their respective domain edges to

Table 1
Full List of Submodels in CSEM2

Model/Region	Publication	Minimum period [s]	Source-receiver pairs
PREM	Dziewonski and Anderson (1981)	–	–
S20RTS	Ritsema et al. (1999)	–	–
Crustal Model	Meier et al. (2007)	55	–
South Atlantic	Colli et al. (2013)	55	2,992
Australasia	Fichtner et al. (2010)	30	3,833
Wider Japanese Islands	Simutė et al. (2016)	20	6,917
Europe	Fichtner et al. (2013)	30	14,026
Marmara	Çubuk-Sabuncu et al. (2017)	8	2,649
Iberia	Fichtner and Villaseñor (2015)	12	8,182
North Atlantic	Rickers et al. (2013)	25	4,103
North America	Krischer et al. (2018)	30	78,510
Japan	Fichtner and Simutė (2018)	15	2,604
Eastern Mediterranean	Blom et al. (2020)	28	10,575
1st Global Inversion	Fichtner et al. (2018)	50	33,227
Iran	Masouminia et al. (2024)	20	2,919
Africa	van Herwaarden et al. (2023)	35	32,412
Central Andes	Gao et al. (2021)	12	9,140
Asia	Ma et al. (2022)	30	523,435
Southeast Asia	Wehner, Blom, et al. (2022)	20	18,588
Western US	Rodgers et al. (2022)	20	39,164
LOWE	Thrastarson et al. (2024a)	50	4,925,373
2nd Global Inversion	*This study*	50	6,041,095

Note. The submodels are arranged sequentially based on their incorporation during the assembly of CSEM2. Minimum periods (if applicable) are provided alongside the original publication. Lines separate the base models, first generation models, and newly incorporated second-generation submodels. Outside the base models, all refinements were obtained with an FWI approach.

avoid the introduction of artificial discontinuities. We found that a cosine-taper width of 4 wavelengths is sufficient to avoid reflections at submodel boundaries within the assembled CSEM. Moreover, the parametrization approach with tapers and updates to the previous version preserves the 1D structure of the submodels in the CSEM without requiring explicit meshing of discontinuities.

2.2. Second-Generation Submodels

CSEM2 includes 22 global- and regional-scale Earth models, listed in Table 1 in the order in which they have been incorporated. With the exception of the base models, all of the submodels were developed with an FWI workflow.

This study integrates seven recent independently obtained seismic tomography models within CSEM2. These new refinements are diverse in scale and spatial resolution and significantly extend the volume of data included in CSEM1 (see Figure 1, Table 1). Collectively, the submodels include a total of 793,276 unique source-receiver pairs. The two continental-scale contributions for Asia by Ma et al. (2022) and Africa by van Herwaarden et al. (2023) have substantially improved the coverage on their respective continents. Additionally, local contributions in Iran (Masouminia et al., 2024), Southeast Asia (Wehner, Blom, et al., 2022), the Central Andes (Gao et al., 2021), and the Western US (Rodgers et al., 2022) are crucial for enhancing resolution and model earthquake-induced ground motion and constrain earthquake sources on smaller scales of several hundred kilometers.

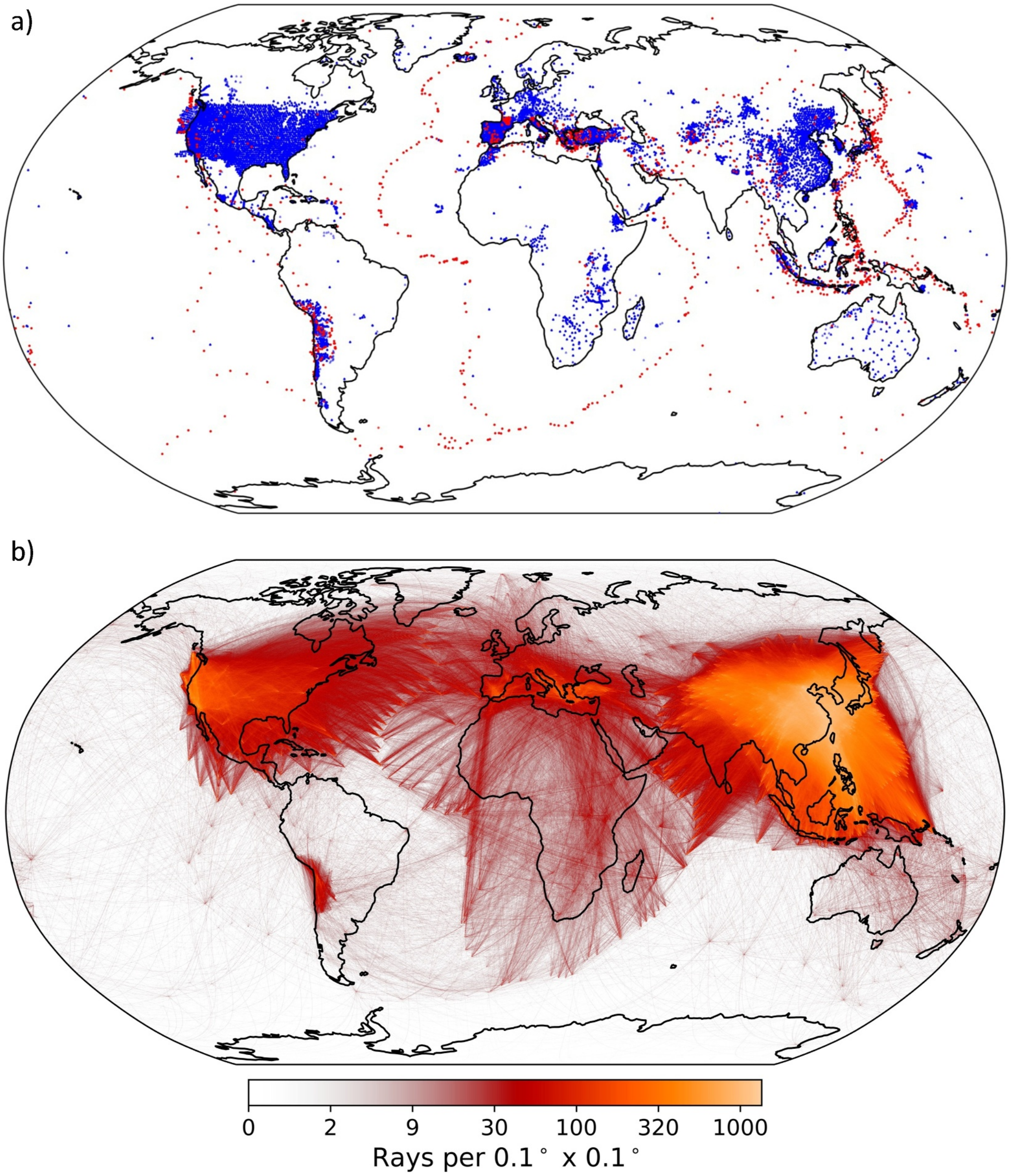

Figure 1. Data in CSEM2 submodels. (a) Locations of the 1,845 earthquakes (red) and 15,422 seismic stations (blue) from all CSEM2 submodels excluding the data for LOWE and the global inversion. (b) Ray density for the same data, visualizing the 793,276 unique source-receiver pairs. Both figures do not incorporate data from LOWE due to the difficulty in identifying which source-receiver pairs specifically contributed to the included areas. Data for the global inversion is excluded but presented in Figure 2a.

Due to the distribution of earthquakes and seismic sensors globally, imaging remote regions like the Arctic, Antarctica, or the Pacific presents challenges in regional tomographies. To achieve reasonable coverage in these regions, required domain sizes would need to be exceedingly large and practically global scale. For this reason, we incorporated, in part, the global seismic Earth model LOWE (long-wavelength earth model (Thrastarson et al., 2022)) with a minimum period of 50 s (Thrastarson et al., 2024a). To contextualize LOWE, we removed the combined area of all previous CSEM submodels, only including the remaining volume as a new submodel. Because it is non-trivial to determine which source-receiver pairs specifically contributed to the included areas of LOWE, the data depicted in Figure 1 exclude those used for the construction of LOWE. As an FWI-based model with a parametrization compatible with our methodology (e.g., attenuation, anisotropy, or bathymetry), LOWE is well suited for our purposes and can be seamlessly integrated into the framework.

3. Global Inversion

3.1. Motivation

While each regional tomographic model more or less accurately describes wave propagation in its respective domain, their compilation into a global model requires the effective combination of the information contained in each of the models. Incorporating teleseismic data may improve resolution at regional scale. Conversely, well-resolved crustal and uppermost mantle structures in regional submodels help to improve the recovery of the deeper mantle, which is usually excluded in regional tomographic studies. Moreover, wave propagation through domain boundaries between tomographic models with different resolutions leads to inevitable interactions with the wavefield (Ajala & Persaud, 2021, 2022; Muir et al., 2022), a complication we have addressed with tapers around the submodels (see Section 2.1). The global inversion corrects inconsistencies arising from such a coarse approach and ensures a coherent final Earth model. In the construction of CSEM2, we focus on reconciling all contributing models with a wave fit on a global scale at a minimum period of 50 s.

3.2. Data Set

The data set used in the inversion and for validation is displayed in Figure 2a. We downloaded publicly available seismic waveforms from 2,423 earthquakes from 1976 to 2021 in the moment magnitude range 5.9–6.9 from the FDSN web services (Romanowicz & Dziewonski, 1986) through the interface of *ObsPy* (Beyreuther et al., 2010; Krischer et al., 2015). Earthquake records in the data set extend for 1 hr after the source time to capture global seismic body wave phases. The total number of unique source-receiver pairs in the data set amounts to 6,041,095. The upper bound on the magnitude range is related to the point-source approximation, as large events above M7 tend to have a source duration longer than our minimum period (Vallée & Douet, 2016). Moreover, earthquakes in our magnitude range display typical rupture lengths on the order of 10–100 km (Wells & Coppersmith, 1994), well below simulated wavelengths. Recordings of small earthquakes, on the other hand, are below the signal-to-noise ratio for distant receivers. The M5.9 threshold has proven robust in maximizing the data available for each event. Moment tensor solutions are taken from the Global Centroid Moment Tensor (GCMT) catalog (Ekström et al., 2012). We select 75 quasi-randomly distributed earthquakes as validation events for which we compute the misfits at every fourth iteration. As these events never contribute to the gradient computation, they serve as an independent monitoring device to verify that the model updates improve waveform fits and inform about progress and convergence per period band.

3.3. Inversion Strategy

In the global inversion, we take advantage of dynamic mini-batches (van Herwaarden et al., 2020), which reduce data redundancy in gradient computations by quasi-randomly batching the data set per iteration. A quarter of the events per batch is carried over to the next iteration to ensure that the last update has improved the misfit. The size of the mini-batches adapts dynamically, finding a balance between increasing accuracy of the gradient and decreasing the size of the batch per iteration during the inversion process. By employing batch sizes ranging from 50 to 200 events, this approach reduces the total number of simulations per iteration by a factor of 10–40 for this data set in comparison to a traditional full-batch approach. However, it can be expected that any given misfit reduction requires more iterations with the mini-batch approach than with the full data set, leading to a larger number of iterations in the inversion while keeping the total number of simulations low (van Herwaarden et al., 2020). Another strategy that we employ to reduce computing costs is event-adaptive meshing (Thrastarson et al., 2020; van Driel et al., 2020). Instead of basing the spectral-element mesh on a cubed-sphere (Komatitsch & Tromp, 2002), the elements are arranged radially symmetric around the source, exploiting the fact that the wavelength in the radial direction of propagation is significantly shorter compared to the azimuthal direction. Accurate gradients are computed on the basis of the discrete adjoint method, overcoming the apparent complication of not having meshes centered at the positions of adjoint sources (Thrastarson et al., 2020; van Driel et al., 2020). Even though event-adaptive meshes require two separate interpolation steps per event, once after the mesh creation for the forward simulation, and a second time for the gradient to project it back onto the original mesh, the time saving during individual simulations far outweighs the costs of the interpolations (Thrastarson et al., 2020, 2024b). Combining the mini-batches and the event-adapted meshes reduces the numerical costs by at least an order of magnitude, rendering the global inversion at 50 s minimum period feasible with a large global data set.

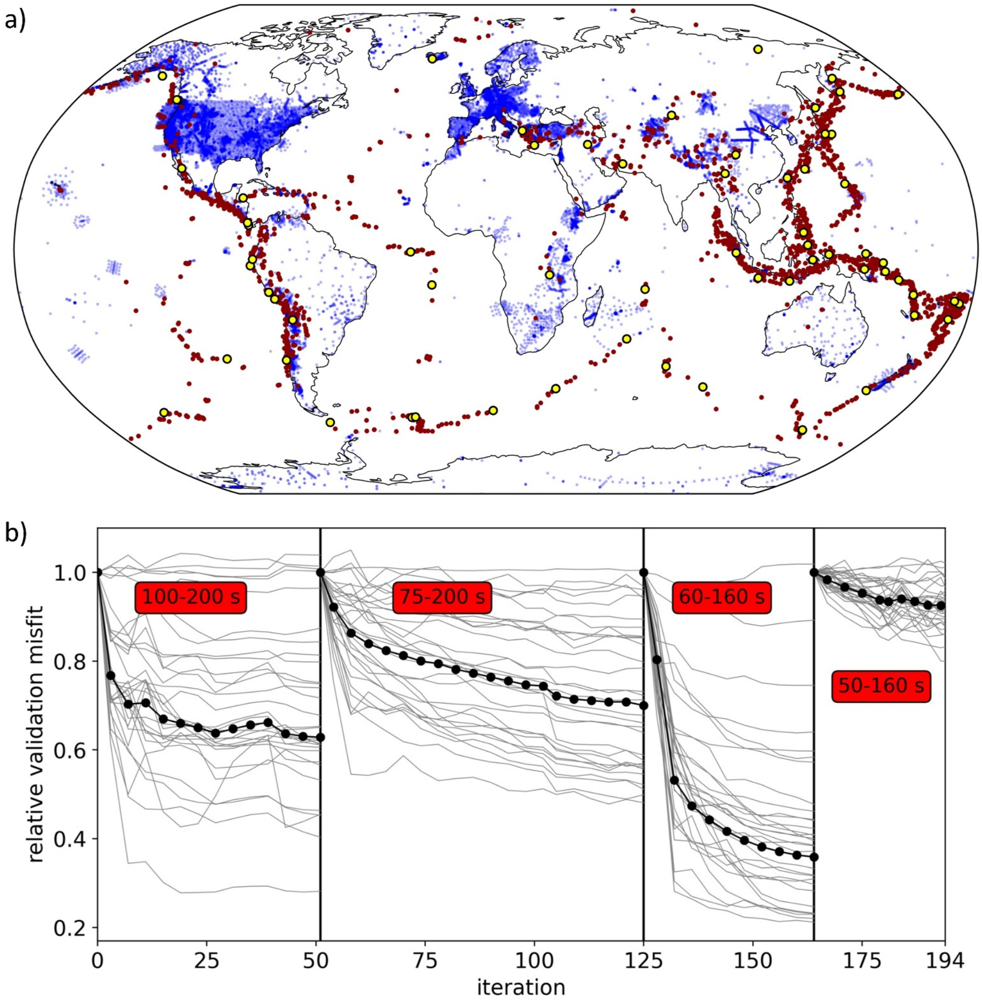

Figure 2. Global inversion data set and misfit reduction. (a) Data set of the global inversion. 2,423 earthquakes (red) and 30,538 seismic stations (blue). The 75 validation events (yellow) provide an independent test for model performance throughout the inversion analyzed in (b). (b) Validation misfit history over the course of the inversion for each of the four period bands for all validation events combined (black line) and for individual events (gray lines). The global inversion encompasses a total of 194 iterations.

The workflow minimizes the objective function based on phase differences in the time-frequency domain, a common choice in seismological FWI problems (Fichtner et al., 2009) and used in many submodels included in this study. Model updates are derived with an Adaptive Moment Estimation (ADAM) approach (Kingma & Ba, 2014). ADAM optimizes models by incorporating the momentum of gradients and efficiently updating model parameters based on a combination of past gradients and their respective squared gradients. ADAM is well-suited for stochastic iterative optimization due to its ability to handle non-stationary objective functions like in the dynamic mini-batch approach. The non-stationary characteristic complements the introduction of a validation data set to test model improvements on a stationary quantity.

The automated data processing steps involve removing the instrument response from the raw data, applying a bandpass filter, and defining measurement windows for each period band. With the tools provided by the *LASIF* package (Thrastarson, van Herwaarden, Krischer, & Fichtner, 2021), we select and include only waveforms with a sufficiently small difference in phase arrivals between the observed and synthetic seismograms to prevent cycle skipping and focus on traces with a good signal-to-noise ratio. To compensate for unequal distribution of receivers, we apply station weighting by distance (Ruan et al., 2019) to give more weight to isolated receivers in the gradient computation. All workflow stages were executed on an HPC cluster, encompassing data processing, event-specific mesh generation, model interpolations, and gradient computation. We used the *Salvus* software

(Afanasiev et al., 2019) for spectral-element simulations, and automate the inversion and HPC-communication with the *Inversionson* package (Thrastarson, van Herwaarden, & Fichtner, 2021). Numerical simulations account for topography and bathymetry, where the ocean is approximated by an equivalent ocean load instead of simulating the fluid ocean explicitly, a valid assumption for periods longer than 50 s (Wehner, Rawlinson, et al., 2022).

The starting model of the global inversion is the first-generation CSEM after incorporation of all second-generation regional refinements (see Table 1). P-wave speeds, anisotropic S-wave speeds, and density in the Earth's crust and mantle are the target of the inversion. The crust, particularly the Moho-discontinuity depth, is not meshed explicitly in our full-waveform simulations. This enables the inversion to dictate where the wave speeds near the Moho need to be adjusted, albeit with smooth updates in crust and upper mantle. We employ a multi-scale approach (Bunks et al., 1995), which involves a gradual increase in shorter-period content as the iterations progress across four period bands: 100–200 s, 75–200 s, 60–160 s, and 50–160 s.

3.4. Inversion Process

As illustrated in Figure 2b, the first period band (100–200 s) shows a strong initial misfit reduction. This indicates that our updating scheme imposes substantial adjustments to the global-scale structure in newly added regions, where long wavelengths were not constrained by their respective inversions. Despite increasing batch sizes and the number of azimuthal elements, validation misfits begin to stagnate after about 30 iterations, prompting the conclusion of the first period band. During the second period band (75–200 s), the misfit is further steadily reduced. Between period bands 2 and 3, the maximum period is reduced from 200 to 160 s, assuming convergence of large-scale structure above 160 s. This relatively minor reduction in the maximum period enables the window picker to select more windows, increasing the total amount of considered data and leading to an estimated increase of 15% in total seismic stations. The third period band (60–160 s) reduces the misfit significantly, down to 36% relative to the starting misfit. The last period band, with minimum periods of 50 s, ceases to find valuable model updates after only a handful of iterations. Despite manual adjustments to batch sizes and simulation mesh resolution, we concluded the global inversion with this period band after a total of 194 iterations and total compute costs of approximately 90,000 node hours. In a final step to produce CSEM2, we compute the wave speed and density difference of the resulting model at 50 s minimum period relative to the starting model. The global update becomes the final item in the list of refinements within the CSEM2 library.

4. Model Presentation and Assessment

4.1. Depth Slices

We inspect the resulting model for consistency with expected features. Figures 3a and 3b present wave speeds of vertically polarized S-waves (VSV) around the globe at 100 km depth for the first-generation CSEM and CSEM2 constructed in this study. They serve as an illustration of the extensive coverage of CSEM2, with anomalies of variable scale lengths around the globe and more detailed compared to CSEM1. Overall, the imaged structures significantly vary in size, reflecting the multi-scale aspect of the model, with small-scale structures visible in regions covered by submodels like Western US, Central Andes, the Eastern Mediterranean, and Southeast Asia. Structures below the Pacific and the polar regions are of larger size, but nevertheless are an improvement from the state of the previous generation where the last refinement in remote areas corresponded to large-scale structures in S20RTS (Ritsema et al., 1999).

Figures 3c–3f zoom into different areas of CSEM2, revealing the short-period structures of the various submodels including fast anomalies below Chile, Eastern and Southeastern Asia, and the US-Pacific Northwest, revealing subducting plates. The long, elongated fast anomaly below Sumatra and Java (Figure 3d), indicating a subducting plate, is imaged spanning multiple submodels, suggesting consistency within the construction of CSEM2. Most hotspot locations from the catalog of Courtillot et al. (2003) are associated with slow VSV-anomalies as expected. Slices for more regions, depths and model parameters can be found in the supplement. For further interpretation, we refer the reader to the original publications of the submodels.

Images of the model within deeper parts of the mantle for isotropic P-wave speed (VP) and VSV are presented in Figure 4. Within CSEM2, the length scale of resolved structures varies significantly based on whether a submodel extends deep enough in a given area, which is particularly noticeable when comparing Eastern Asia to its

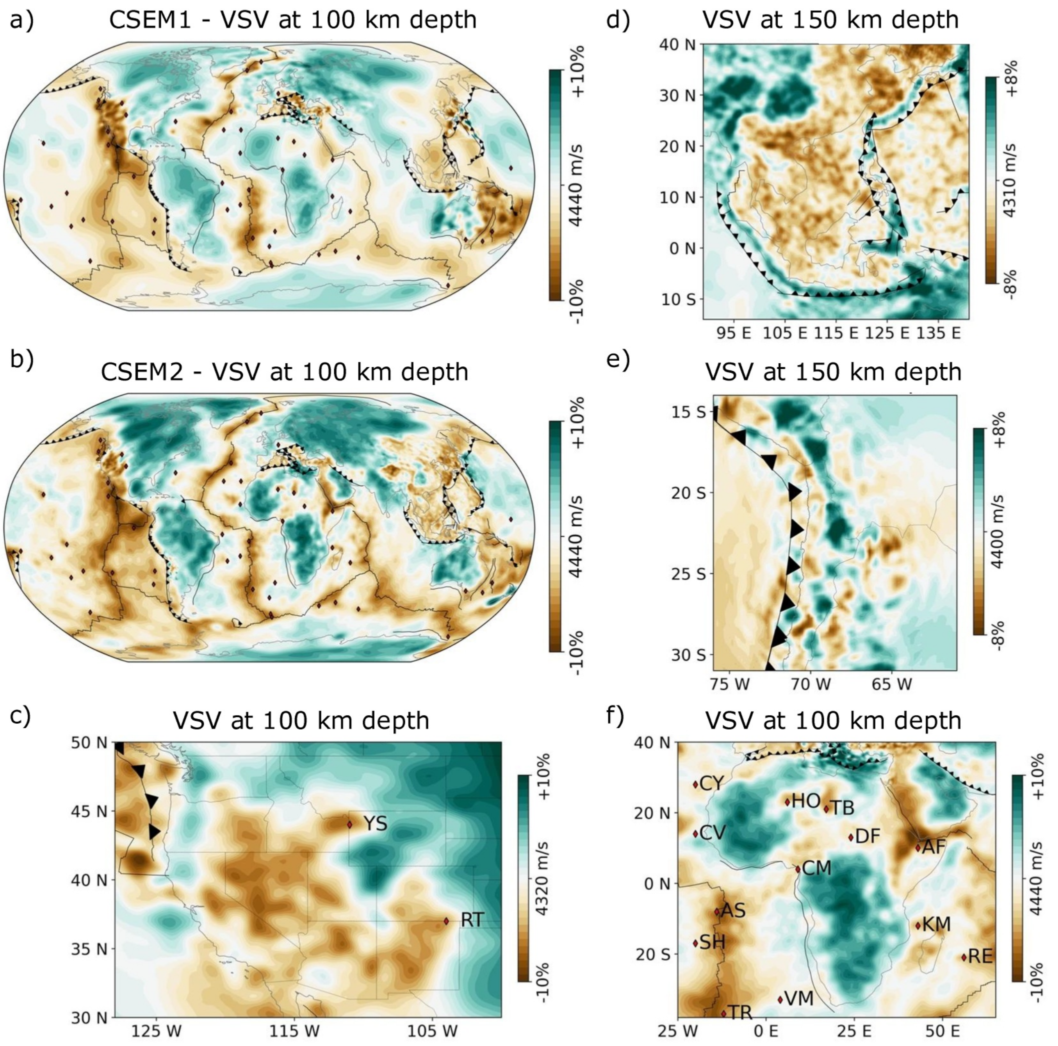

Figure 3. Depth slices for CSEM2. (a) CSEM1 on the global scale for comparison, (b) CSEM2 with global coverage in contrast to CSEM1. (c–f) CSEM2 depth slices highlighting various regions. All subfigures depict vertically polarized S-wave speed (VSV). Plate boundaries including subduction zones from Müller et al. (2019) and drawn using *GPlately* (Müller et al., 2018). Hotspots indicated by red diamonds taken from the catalog in Courtillot et al. (2003). More depth slices for other regions and model parameters can be found in the supplement. Abbreviations: AF, Afar; AS, Ascension; CM, Cameroon; CY, Canary; DF, Darfur; HO, Hoggar; KM, Comores; RE, La Réunion; RT, Raton; SH, St Helena; TB, Tibesti; TR, Tristan; VM, Vema; YS, Yellowstone.

surroundings. The fast anomaly associated with a subducting plate beneath South America is consistently observed throughout the mantle in VSV, while it is less prominent in the VP model. VP typically exhibits longer resolved length scales, which is expected for the periods where FWI typically operates in global and regional-scale studies. Nevertheless, many hotspot locations correspond to slow VP anomalies in the upper mantle and transition zone. The presented depth slices throughout the mantle illustrate that the workflow of CSEM2 leads to a multi-parameter, multi-scale global Earth model.

4.2. Model Assessment

In the following, we provide evidence that numerical simulations using CSEM2 indeed conform to observations and that the global updates did not sacrifice the local waveform fit of the smaller-scale regional models. For a quantitative comparison, we compute the relative improvement of the root-mean squared L_2 misfit (amplitude residuals) from PREM (Dziewonski & Anderson, 1981) to CSEM2 on the full seismic traces without window

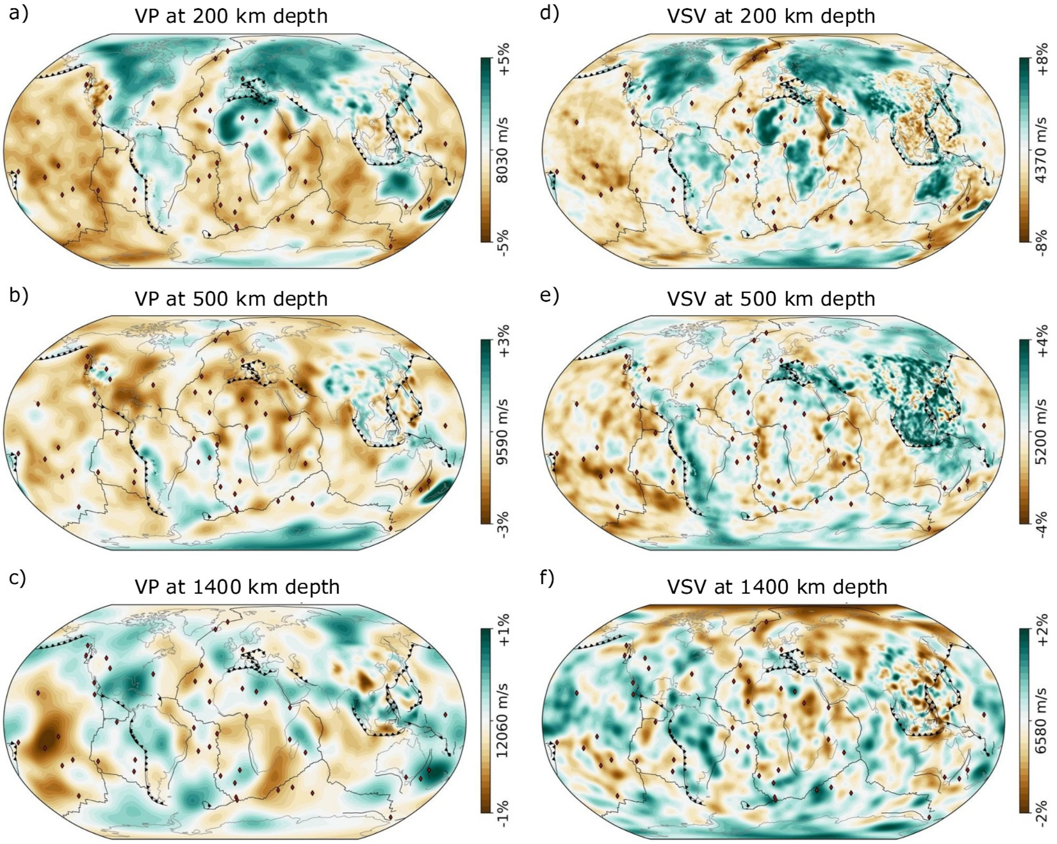

Figure 4. CSEM2 within the mantle: (a–c) isotropic P-wave speed in the upper mantle, transition zone, and lower mantle; (d–f) VSV for the same depth slices. Descriptions of plate boundaries and hotspots (red markers) are provided in Figure 3. These features are shown at their surface location.

picking. To emphasize high-quality traces for the comparison, we normalize the misfits with the noise level where the noise per station is estimated on 2 hr of data before source time.

On the global scale, we visually analyze waveforms at seismic stations distributed around the globe at 50–160 s for a validation event from the global inversion in Figure 5a. The validation event is located in central Africa, and therefore within one of the submodels. The observations largely agree with the computed displacements at seismic stations, despite the elastic waves entering and passing through various regional refinements. The 3D heterogeneities introduced by the CSEM2-submodels and the global inversion benefit the wave propagation, as illustrated with the waveform difference relative to PREM (Dziewonski & Anderson, 1981). On two global networks, GEOSCOPE (Leroy et al., 2023) and GEOFON (Quinteros et al., 2021), amplitude residuals have improved over PREM by 57.6% and 37.0%, respectively.

On the regional scale, we test the waveform fit on the Western United States model (WUS256, Rodgers et al., 2022) and the Central Andes model (Gao et al., 2021) added to the CSEM in this study. As illustrated in Figure 5b, the synthetic seismograms in the Western US match the data throughout the region at 20 s, preserving the shortest period resolved by the model despite the correcting global iterations at 50 s. On 311 receivers from the Southern Californian Seismic Network (Hutton et al., 2010), in the vicinity of the earthquake location, amplitude residuals have been improved by 63.5% over PREM, and by 60.1% on the 20 high-quality stations from the United States National Seismic Network (Benz et al., 2001) in the domain. Even stations outside of the domain of WUS256, in Texas or Nebraska, exhibit improved traveltime residuals in comparison to PREM, validating wave propagation across submodel boundaries. Similarly, the waveform fit at 20 s is retained for the Central Andes refinement (Figure 5c). We observe an overall amplitude residual reduction of 23.6% with respect to PREM for the 42 seismic stations.

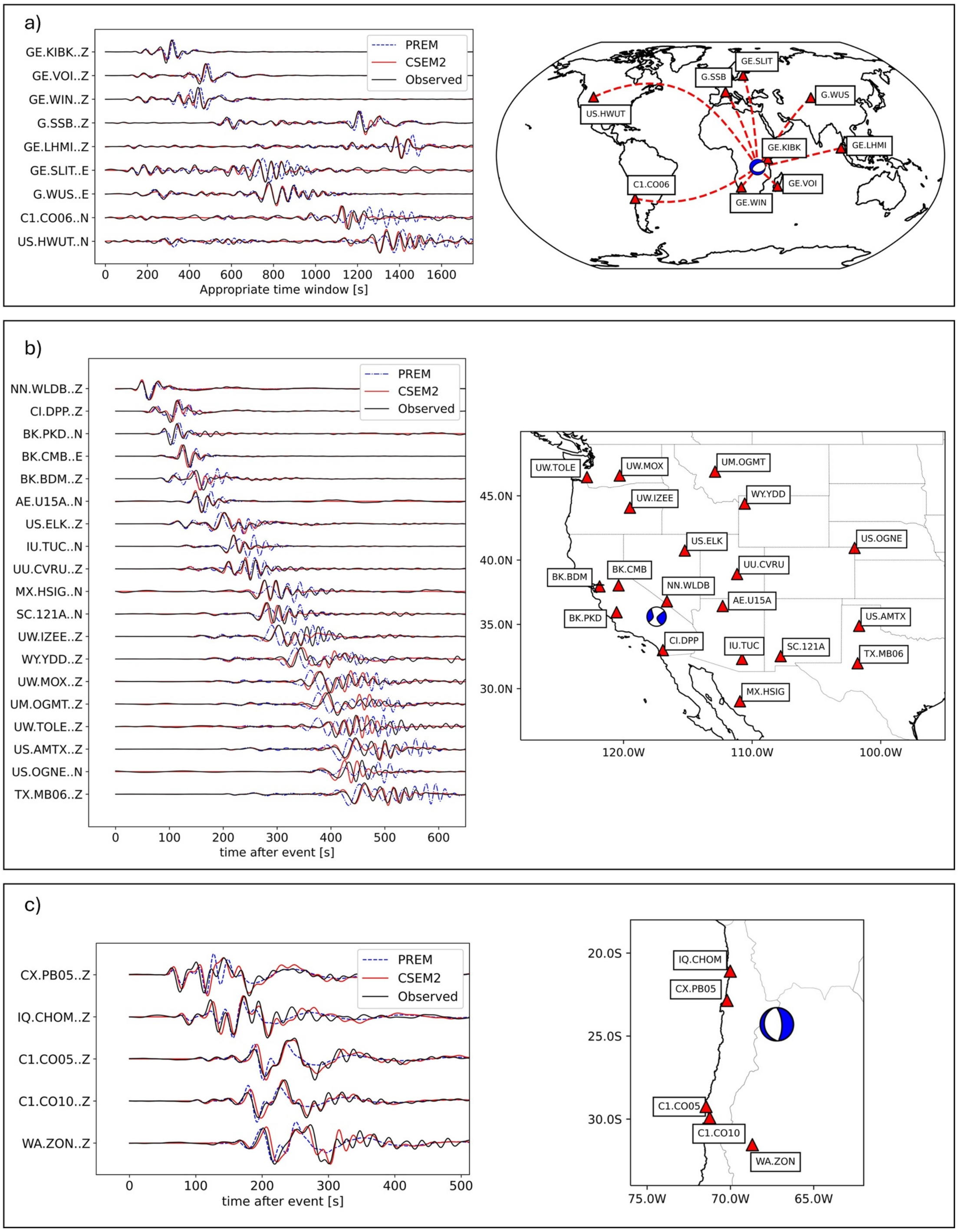

Figure 5. Validation tests. (a) Location of test event and stations for the globe with the comparison of observed and synthetic displacements of a M6.0 earthquake within the validation data set for the final period band (50–160 s). (b) Source and receiver locations for a model test in the Western US with periods 20–160 s for a M5.6 earthquake. (c) Same as (b) for the Central Andes region with a M5.7 earthquake. Synthetic waveforms for PREM are included for comparison. Computed seismograms for CSEM2 and observations largely overlap. The waveform fits suggest that region studies have been successfully embedded into the global model. Waveform amplitudes are rescaled.

The numerical tests confirm the validity of the model across scales and highlight the suitability of CSEM2 for both global and regional applications. The comparison of waveforms computed with CSEM2 to other tomographic models is complicated by the fact that models are not easily transferable between different forward problem solvers, often because of small but numerous implementation details such as the formulation of visco-elastic attenuation, topographic and bathymetric models, modeling of the ocean layer, and many others. Therefore, we provide a library of CSEM2 synthetic seismograms computed with Salvus (Afanasiev et al., 2019) for 25 globally distributed earthquakes (Noe et al., 2024). This library is intended to facilitate a quantitative comparison of CSEM2 and Salvus waveform fits to other combinations of Earth models and forward problem solvers.

5. Discussion

The novelty of the global seismic Earth model constructed in this study lies in its unrestricted nature, not confined to a specific study area and resolution. In theory, regional updates of any scale may be introduced within the framework, making it possible to resolve large-scale mantle structures jointly with the crust. Moreover, to the best of our knowledge, the multi-scale second-generation CSEM encompasses a volume of data unmatched by any other FWI model, as it aims to explain a broader data set than any previous model through the incorporation of regional event data within the submodels. It is constructed with over 6 million unique source-receiver pairs on the global scale, plus another 700,000 ray paths from regional contributions, including earthquakes down to M3.7 (Çubuk-Sabuncu et al., 2017) and therefore significantly below the threshold of our global data set at M5.9. Especially on the global scale, the extensive data set can be managed within an FWI-approach only by combining the dynamic mini-batches with the event adaptive spectral-element meshes.

The test cases presented in Figure 5 provide evidence that the construction of the multi-scale model through larger-scale model updates is a valid approach. The introduction of tapered submodels is analogous to Ajala and Persaud (2022) to avoid artificial discontinuities at submodel boundaries. The significant misfit improvement during the global full-waveform approach suggests that the taper itself does not suffice to describe wave-propagation through submodel boundaries. It indicates that the global-scale updating approach correctly adjusts the structure to incorporate the smaller-scale domain into the global framework.

This updating approach, crucial for explaining global wave propagation, introduces a trade-off by necessitating changes to the regional submodels. Unless these changes coincidentally happen to only navigate in the effective nullspace of a regional data set, they must increase the misfit within the respective regional submodel. In our approach we deliberately accept these typically small regional-scale misfit increases in order to strike a balance between those and misfit reductions at global scale. On the one hand, this has the benefit of coupling different scales in CSEM2. On the other hand, it may cause regional or global mono-scale models (e.g., Ciardelli et al., 2022; Cui et al., 2024; French & Romanowicz, 2014; Lei et al., 2020; Ma et al., 2022; Rodgers et al., 2022; Thrastarson et al., 2022, 2024b; Wehner, Blom, et al., 2022) to perform better in terms of waveform fit in the domain where they have been constructed. In the long term, successive iterations between regional- and global-scale refinements in the CSEM should, however, naturally resolve this issue.

Tomographic models derived from FWI have challenges evaluating resolution and uncertainty, and CSEM2 is no exception. In the community, no consensus has been reached on how to comprehensively quantify resolution. Approaches employed by other studies include the computation of point-spread functions (Blom et al., 2020; Fichtner & Trampert, 2011; H. Zhu et al., 2015), randomly probing the model (Fichtner & Leeuwen, 2015), or restitution tests (van Herwaarden et al., 2023), approaches that are either computationally prohibitive for the global model or will be unreasonable for a multi-scale model. Other approaches, such as evaluation of the approximate Hessian during the L-BFGS optimization (Wehner, Blom, et al., 2022), require the availability of all gradients of the local regional tomography models without a straightforward way to implement this information. For these reasons, a conclusive model resolution test spanning the entirety of all CSEM2 regions is not feasible as of now. For model performance, we refer to the validation data set as an independent gauge of model quality, and the consistency of the model with expected geologic features like hotspots and subducting plates.

Future efforts will be directed towards integrating more regional tomographic models into the framework, with a specific emphasis on incorporating higher frequencies. We hope that, at some point, the CSEM can be used to correct for path effects in ground motion modeling. Moreover, the flexibility of the workflow described in Section 2.1 allows us to incorporate wave speed refinements obtained from various sources. In future iterations of the CSEM, we aim to enhance the methodological approach by further refining models using ambient seismic noise tomography (Sager et al., 2020) and incorporating attenuation within the inverted model (Karaoğlu & Romanowicz, 2018). Additionally, we can improve the model by leveraging more data, considering second orbits in global inversions to increase coverage in remote areas, and including measurements from fiber-optic cables (Wuestefeld et al., 2023).

6. Conclusions

CSEM2 encompasses a multi-scale global seismic Earth model facilitated by a collaborative effort and consistently builds on prior knowledge to jointly resolve mantle and crust. The current generation enhances the spatial coverage of submodels in comparison to the first generation, incorporating multiple recent high-resolution studies at regional scales. Consistency is ensured via a data-rich global FWI over four blended period bands, smoothing over regional boundaries to create a model that is consistent across scales. Model performance during the global inversion process is evaluated using an independent data set of validation earthquakes. As such, CSEM2 has the capability to explain wave propagation at 50 s minimum period on the global scale, while simultaneously explaining wave propagation for lower periods in submodel regions. Given that tomographic images offer highly detailed, informative insights into the composition and structure of the Earth's interior, we believe our model holds substantial value for various branches of Earth sciences beyond seismology, including geodynamics, mineralogy, and tectonics. We hope to expand CSEM2 in the future with more refinements and encourage further community collaboration.

Data Availability Statement

Example waveforms from our inversion data set for earthquakes recorded at global seismic stations computed with CSEM2 and Salvus (Afanasiev et al., 2019) are provided as a data set (Noe et al., 2024) to be reproduced independently of the numerical wave propagation solver. Global and regional versions of CSEM2 will be made available at the Earth Model Collaboratory EarthScope (2024). For extractions in specific user-defined domains, please contact the corresponding author, specifying the desired resolution and the latitude, longitude, and depth ranges. The data set used in the global inversion is publicly available through FDSN services (Romanowicz & Dziewonski, 1986) and accessed through the mass downloader within the *ObsPy* package (Krischer et al., 2018).

Acknowledgments
We thank two anonymous reviewers for their insightful comments, which greatly improved this manuscript. The research leading to these results received support from the European Union's (EU) Horizon 2020 research and innovation program through the European Research Council (ERC) Starting Grant, entitled "The Collaborative Seismic Earth Model" (Grant 714069). S.N. gratefully acknowledges funding provided by the European Union's Horizon 2020 research and innovation program under the Marie Skłodowska-Curie grant agreement No. 955515 (SPIN ITN). In addition, the research was supported by the EU project A Digital Twin for Geophysical Extremes (DT-GEO) and has received funding from Horizon Europe under Grant Agreement No. 101058129. The authors express their deep gratitude to the Swiss National Supercomputing Centre (CSCS) for providing computing time under Grant s1168. Work of A.R. was performed under the auspices of the U.S. Department of Energy by Lawrence Livermore National Laboratory under Contract DE-AC52-07NA27344.

References

Afanasiev, M., Boehm, C., van Driel, M., Krischer, L., Rietmann, M., May, D. A., et al. (2019). Modular and flexible spectral-element waveform modelling in two and three dimensions. *Geophysical Journal International*, *216*(3), 1675–1692. https://doi.org/10.1093/gji/ggy469

Ajala, R., & Persaud, P. (2021). Effect of merging multiscale models on seismic wavefield predictions near the southern San Andreas fault. *Journal of Geophysical Research: Solid Earth*, *126*(10), e2021JB021915. https://doi.org/10.1029/2021jb021915

Ajala, R., & Persaud, P. (2022). Ground-motion evaluation of hybrid seismic velocity models. *The Seismic Record*, *2*(3), 186–196. https://doi.org/10.1785/0320220022

Amaru, M. (2007). *Global travel time tomography with 3-D reference models* (p. 274). Utrecht University.

Benz, H., Buland, R., Filson, J., Frankel, A., & Shedlock, K. (2001). The advanced national seismic system. *Seismological Research Letters*, *72*(1), 70–75. https://doi.org/10.1785/gssrl.72.1.70

Beyreuther, M., Barsch, R., Krischer, L., Megies, T., Behr, Y., & Wassermann, J. (2010). ObsPy: A Python toolbox for seismology. *Seismological Research Letters*, *81*(3), 530–533. https://doi.org/10.1785/gssrl.81.3.530

Blom, N., Gokhberg, A., & Fichtner, A. (2020). Seismic waveform tomography of the central and eastern Mediterranean upper mantle. *Solid Earth*, *11*(2), 669–690. https://doi.org/10.5194/se-11-669-2020

Bott, J., Scheck-Wenderoth, M., Kumar, A., Cacace, M., Noe, S., & Faleide, J. I. (2024). Density and strength variations in the mantle lithosphere affect the distribution of intraplate earthquakes. *Communications Earth & Environment*, *5*(1), 243. https://doi.org/10.1038/s43247-024-01417-4

Bunge, H.-P., Hagelberg, C., & Travis, B. (2003). Mantle circulation models with variational data assimilation: Inferring past mantle flow and structure from plate motion histories and seismic tomography. *Geophysical Journal International*, *152*(2), 280–301. https://doi.org/10.1046/j.1365-246x.2003.01823.x

Bunks, C., Saleck, F. M., Zaleski, S., & Chavent, G. (1995). Multiscale seismic waveform inversion. *Geophysics*, *60*(5), 1457–1473. https://doi.org/10.1190/1.1443880

Chaljub, E., Moczo, P., Tsuno, S., Bard, P.-Y., Kristek, J., Käser, M., et al. (2010). Quantitative comparison of four numerical predictions of 3D ground motion in the Grenoble valley, France. *Bulletin of the Seismological Society of America*, *100*(4), 1427–1455. https://doi.org/10.1785/0120090052

Ciardelli, C., Assumpção, M., Bozdağ, E., & van der Lee, S. (2022). Adjoint waveform tomography of South America. *Journal of Geophysical Research: Solid Earth*, *127*(2), e2021JB022575. https://doi.org/10.1029/2021jb022575

Colli, L., Fichtner, A., & Bunge, H.-P. (2013). Full waveform tomography of the upper mantle in the South Atlantic region: Imaging a westward fluxing shallow asthenosphere? *Tectonophysics*, *604*, 26–40. https://doi.org/10.1016/j.tecto.2013.06.015

Courtillot, V., Davaille, A., Besse, J., & Stock, J. (2003). Three distinct types of hotspots in the Earth's mantle. *Earth and Planetary Science Letters*, *205*(3–4), 295–308. https://doi.org/10.1016/s0012-821x(02)01048-8

Çubuk-Sabuncu, Y., Taymaz, T., & Fichtner, A. (2017). 3-D crustal velocity structure of western Turkey: Constraints from full-waveform tomography. *Physics of the Earth and Planetary Interiors*, *270*, 90–112. https://doi.org/10.1016/j.pepi.2017.06.014

Cui, C., Lei, W., Liu, Q., Peter, D., Bozdağ, E., Tromp, J., et al. (2024). GLAD-M35: A joint P and S global tomographic model with uncertainty quantification. *Geophysical Journal International*, *239*(1), 478–502. https://doi.org/10.1093/gji/ggae270

Dahlen, F., Hung, S.-H., & Nolet, G. (2000). Fréchet kernels for finite-frequency traveltimes—I. Theory. *Geophysical Journal International*, *141*(1), 157–174. https://doi.org/10.1046/j.1365-246x.2000.00070.x

Donner, S., Mustac, M., Hejrani, B., Tkalčić, H., & Igel, H. (2020). Seismic moment tensors from synthetic rotational and translational ground motion: Green's functions in 1-D versus 3-D. *Geophysical Journal International*, *223*(1), 161–179. https://doi.org/10.1093/gji/ggaa305

Dziewonski, A. M., & Anderson, D. L. (1981). Preliminary reference Earth model. *Physics of the Earth and Planetary Interiors*, *25*(4), 297–356. https://doi.org/10.1016/0031-9201(81)90046-7

EarthScope. (2024). *Data Services Products: EMC-EarthModels* [Model]. Incorporated Research Institutions for Seismology. https://ds.iris.edu/ds/products/emc-earthmodels/

Ekström, G., Nettles, M., & Dziewoński, A. (2012). The global CMT project 2004–2010: Centroid-moment tensors for 13,017 earthquakes. *Physics of the Earth and Planetary Interiors*, *200*, 1–9. https://doi.org/10.1016/j.pepi.2012.04.002

Fichtner, A., Bunge, H.-P., & Igel, H. (2006). The adjoint method in seismology: I. Theory. *Physics of the Earth and Planetary Interiors*, *157*(1–2), 86–104. https://doi.org/10.1016/j.pepi.2006.03.016

Fichtner, A., Kennett, B. L., Igel, H., & Bunge, H.-P. (2009). Full seismic waveform tomography for upper-mantle structure in the Australasian region using adjoint methods. *Geophysical Journal International*, *179*(3), 1703–1725. https://doi.org/10.1111/j.1365-246x.2009.04368.x

Fichtner, A., Kennett, B. L., Igel, H., & Bunge, H.-P. (2010). Full waveform tomography for radially anisotropic structure: New insights into present and past states of the Australasian upper mantle. *Earth and Planetary Science Letters*, *290*(3–4), 270–280. https://doi.org/10.1016/j.epsl.2009.12.003

Fichtner, A., & Leeuwen, T. V. (2015). Resolution analysis by random probing. *Journal of Geophysical Research: Solid Earth*, *120*(8), 5549–5573. https://doi.org/10.1002/2015jb012106

Fichtner, A., & Simutė, S. (2018). Hamiltonian Monte Carlo inversion of seismic sources in complex media. *Journal of Geophysical Research: Solid Earth*, *123*(4), 2984–2999. https://doi.org/10.1002/2017jb015249

Fichtner, A., & Trampert, J. (2011). Resolution analysis in full waveform inversion. *Geophysical Journal International*, *187*(3), 1604–1624. https://doi.org/10.1111/j.1365-246x.2011.05218.x

Fichtner, A., Trampert, J., Cupillard, P., Saygin, E., Taymaz, T., Capdeville, Y., & Villasenor, A. (2013). Multiscale full waveform inversion. *Geophysical Journal International*, *194*(1), 534–556. https://doi.org/10.1093/gji/ggt118

Fichtner, A., van Herwaarden, D.-P., Afanasiev, M., Simutė, S., Krischer, L., Çubuk-Sabuncu, Y., et al. (2018). The Collaborative Seismic Earth Model: Generation 1. *Geophysical Research Letters*, *45*(9), 4007–4016. https://doi.org/10.1029/2018gl077338

Fichtner, A., & Villaseñor, A. (2015). Crust and upper mantle of the western Mediterranean–constraints from full-waveform inversion. *Earth and Planetary Science Letters*, *428*, 52–62. https://doi.org/10.1016/j.epsl.2015.07.038

French, S. W., & Romanowicz, B. (2014). Whole-mantle radially anisotropic shear velocity structure from spectral-element waveform tomography. *Geophysical Journal International*, *199*(3), 1303–1327. https://doi.org/10.1093/gji/ggu334

Gallovič, F., Käser, M., Burjánek, J., & Papaioannou, C. (2010). Three-dimensional modeling of near-fault ground motions with nonplanar rupture models and topography: Case of the 2004 Parkfield earthquake. *Journal of Geophysical Research*, *115*(B3), B03308. https://doi.org/10.1029/2008jb006171

Gao, Y., Tilmann, F., van Herwaarden, D.-P., Thrastarson, S., Fichtner, A., Heit, B., et al. (2021). Full waveform inversion beneath the Central Andes: Insight into the dehydration of the Nazca slab and delamination of the back-arc lithosphere. *Journal of Geophysical Research: Solid Earth*, *126*(7), e2021JB021984. https://doi.org/10.1029/2021jb021984

Graves, R. W., & Pitarka, A. (2010). Broadband ground-motion simulation using a hybrid approach. *Bulletin of the Seismological Society of America*, *100*(5A), 2095–2123. https://doi.org/10.1785/0120100057

Hejrani, B., Tkalčić, H., & Fichtner, A. (2017). Centroid moment tensor catalogue using a 3-D continental scale Earth model: Application to earthquakes in Papua New Guinea and the Solomon Islands. *Journal of Geophysical Research: Solid Earth*, *122*(7), 5517–5543. https://doi.org/10.1002/2017jb014230

Hingee, M., Tkalčić, H., Fichtner, A., & Sambridge, M. (2011). Seismic moment tensor inversion using a 3-D structural model: Applications for the Australian region. *Geophysical Journal International*, *184*(2), 949–964. https://doi.org/10.1111/j.1365-246x.2010.04897.x

Hjörleifsdóttir, V., & Ekström, G. (2010). Effects of three-dimensional Earth structure on CMT earthquake parameters. *Physics of the Earth and Planetary Interiors*, *179*(3–4), 178–190. https://doi.org/10.1016/j.pepi.2009.11.003

Hutton, K., Woessner, J., & Hauksson, E. (2010). Earthquake monitoring in southern California for seventy-seven years (1932–2008). *Bulletin of the Seismological Society of America*, *100*(2), 423–446. https://doi.org/10.1785/0120090130

Karaoğlu, H., & Romanowicz, B. (2018). Global seismic attenuation imaging using full-waveform inversion: A comparative assessment of different choices of misfit functionals. *Geophysical Journal International*, *212*(2), 807–826. https://doi.org/10.1093/gji/ggx442

Kingma, D. P., & Ba, J. (2014). Adam: A method for stochastic optimization. *arXiv preprint arXiv:1412.6980*.

Koelemeijer, P., Deuss, A., & Ritsema, J. (2013). Observations of core-mantle boundary Stoneley modes. *Geophysical Research Letters*, *40*(11), 2557–2561. https://doi.org/10.1002/grl.50514

Komatitsch, D., Liu, Q., Tromp, J., Suss, P., Stidham, C., & Shaw, J. H. (2004). Simulations of ground motion in the Los Angeles basin based upon the spectral-element method. *Bulletin of the Seismological Society of America*, *94*(1), 187–206. https://doi.org/10.1785/0120030077

Komatitsch, D., & Tromp, J. (2002). Spectral-element simulations of global seismic wave propagation—I. Validation. *Geophysical Journal International*, *149*(2), 390–412. https://doi.org/10.1046/j.1365-246x.2002.01653.x

Krischer, L., Fichtner, A., Boehm, C., & Igel, H. (2018). Automated large-scale full seismic waveform inversion for North America and the North Atlantic. *Journal of Geophysical Research: Solid Earth*, *123*(7), 5902–5928. https://doi.org/10.1029/2017jb015289

Krischer, L., Megies, T., Barsch, R., Beyreuther, M., Lecocq, T., Caudron, C., & Wassermann, J. (2015). ObsPy: A bridge for seismology into the scientific Python ecosystem. *Computational Science & Discovery*, *8*(1), 014003. https://doi.org/10.1088/1749-4699/8/1/014003

Lailly, P., & Bednar, J. (1983). The seismic inverse problem as a sequence of before stack migrations. In *Conference on inverse scattering: theory and application* (Vol. 1983, pp. 206–220).

Lei, W., Ruan, Y., Bozdağ, E., Peter, D., Lefebvre, M., Komatitsch, D., et al. (2020). Global adjoint tomography—Model GLAD-M25. *Geophysical Journal International*, *223*(1), 1–21. https://doi.org/10.1093/gji/ggaa253

Leroy, N., Vallée, M., Zigone, D., Romanowicz, B., Stutzmann, E., Maggi, A., et al. (2023). GEOSCOPE network: 40 yr of global broadband seismic data. *Seismological Research Letters*, *95*(3), 1495–1517. https://doi.org/10.1785/0220230176

Liu, Q., & Tromp, J. (2006). Finite-frequency kernels based on adjoint methods. *Bulletin of the Seismological Society of America*, *96*(6), 2383–2397. https://doi.org/10.1785/0120060041

Lomax, A. J., & Bolt, B. A. (1992). Broadband waveform modelling of anomalous strong ground motion in the 1989 Loma Prieta earthquake using three-dimensional geologic structures. *Geophysical Research Letters*, *19*(19), 1963–1966. https://doi.org/10.1029/92gl02246

Ma, J., Bunge, H.-P., Thrastarson, S., Fichtner, A., Herwaarden, D.-P. V., Tian, Y., et al. (2022). Seismic full-waveform inversion of the crust-mantle structure beneath China and adjacent regions. *Journal of Geophysical Research: Solid Earth*, *127*(9), e2022JB024957. https://doi.org/10.1029/2022jb024957

Marquering, H., Dahlen, F., & Nolet, G. (1999). Three-dimensional sensitivity kernels for finite-frequency traveltimes: The banana-doughnut paradox. *Geophysical Journal International*, *137*(3), 805–815. https://doi.org/10.1046/j.1365-246x.1999.00837.x

Masouminia, N., van Herwaarden, D.-P., Thrastarson, S., Rahimi, H., Igel, H., Krischer, L., et al. (2024). First generation of a three-dimensional tomographic model for the uppermost mantle beneath the Zagros collision zone—Constraints from full-waveform inversion. *Acta Geophysica*, 1–14. https://doi.org/10.1007/s11600-024-01386-4

Meier, U., Curtis, A., & Trampert, J. (2007). Fully nonlinear inversion of fundamental mode surface waves for a global crustal model. *Geophysical Research Letters*, *34*(16), L16304. https://doi.org/10.1029/2007gl030989

Muir, J. B., Clayton, R. W., Tsai, V. C., & Brissaud, Q. (2022). Parsimonious velocity inversion applied to the Los Angeles basin, CA. *Journal of Geophysical Research: Solid Earth*, *127*(2), e2021JB023103. https://doi.org/10.1029/2021jb023103

Müller, R. D., Cannon, J., Qin, X., Watson, R. J., Gurnis, M., Williams, S., et al. (2018). GPlates: Building a virtual Earth through deep time. *Geochemistry, Geophysics, Geosystems*, *19*(7), 2243–2261. https://doi.org/10.1029/2018GC007584

Müller, R. D., Zahirovic, S., Williams, S. E., Cannon, J., Seton, M., Bower, D. J., et al. (2019). A global plate model including lithospheric deformation along major rifts and orogens since the Triassic. *Tectonics*, *38*(6), 1884–1907. https://doi.org/10.1029/2018tc005462

Noe, S., van Herwaarden, D. P., Thrastarson, S., & Fichtner, A. (2024). Dataset related to article ′The Collaborative Seismic Earth Model: Generation 2 [Dataset]. *Zenodo*. https://doi.org/10.5281/ZENODO.11047927

Quinteros, J., Strollo, A., Evans, P. L., Hanka, W., Heinloo, A., Hemmleb, S., et al. (2021). The GEOFON program in 2020. *Seismological Research Letters*, *92*(3), 1610–1622. https://doi.org/10.1785/0220200415

Rickers, F., Fichtner, A., & Trampert, J. (2013). The Iceland–Jan Mayen plume system and its impact on mantle dynamics in the North Atlantic region: Evidence from full-waveform inversion. *Earth and Planetary Science Letters*, *367*, 39–51. https://doi.org/10.1016/j.epsl.2013.02.022

Rietmann, M., Messmer, P., Nissen-Meyer, T., Peter, D., Basini, P., Komatitsch, D., et al. (2012). Forward and adjoint simulations of seismic wave propagation on emerging large-scale GPU architectures. In *Sc'12: Proceedings of the International Conference on High Performance Computing, Networking, Storage and Analysis* (pp. 1–11).

Ritsema, J., Heijst, H. J. V., & Woodhouse, J. H. (1999). Complex shear wave velocity structure imaged beneath Africa and Iceland. *Science*, *286*(5446), 1925–1928. https://doi.org/10.1126/science.286.5446.1925

Rodgers, A., Krischer, L., Afanasiev, M., Boehm, C., Doody, C., Chiang, A., & Simmons, N. (2022). WUS256: An adjoint waveform tomography model of the crust and upper mantle of the Western United States for improved waveform simulations. *Journal of Geophysical Research: Solid Earth*, *127*(7), e2022JB024549. https://doi.org/10.1029/2022jb024549

Romanowicz, B., & Dziewonski, A. (1986). Toward a federation of broadband seismic networks. *Eos, Transactions American Geophysical Union*, *67*(25), 537–542. https://doi.org/10.1029/eo067i025p00541

Ruan, Y., Lei, W., Modrak, R., Örsvuran, R., Bozdağ, E., & Tromp, J. (2019). Balancing unevenly distributed data in seismic tomography: A global adjoint tomography example. *Geophysical Journal International*, *219*(2), 1225–1236. https://doi.org/10.1093/gji/ggz356

Sager, K., Boehm, C., Ermert, L., Krischer, L., & Fichtner, A. (2020). Global-scale full-waveform ambient noise inversion. *Journal of Geophysical Research: Solid Earth*, *125*(4), e2019JB018644. https://doi.org/10.1029/2019jb018644

Simmons, N. A., Myers, S. C., Morency, C., Chiang, A., & Knapp, D. R. (2021). SPiRaL: A multiresolution global tomography model of seismic wave speeds and radial anisotropy variations in the crust and mantle. *Geophysical Journal International*, *227*(2), 1366–1391. https://doi.org/10.1093/gji/ggab277

Simutė, S., Boehm, C., Krischer, L., Gokhberg, A., Vallée, M., & Fichtner, A. (2023). Bayesian seismic source inversion with a 3-D Earth model of the Japanese islands. *Journal of Geophysical Research: Solid Earth*, *128*(1), e2022JB024231. https://doi.org/10.1029/2022jb024231

Simutė, S., Steptoe, H., Cobden, L., Gokhberg, A., & Fichtner, A. (2016). Full-waveform inversion of the Japanese islands region. *Journal of Geophysical Research: Solid Earth*, *121*(5), 3722–3741. https://doi.org/10.1002/2016jb012802

Tarantola, A. (1984). Inversion of seismic reflection data in the acoustic approximation: Geophysics. *Geophysics*, *49*(8), 1259–1266. https://doi.org/10.1190/1.1441754

Thrastarson, S., van Driel, M., Krischer, L., Boehm, C., Afanasiev, M., van Herwaarden, D.-P., & Fichtner, A. (2020). Accelerating numerical wave propagation by wavefield adapted meshes. Part II: Full-waveform inversion. *Geophysical Journal International*, *221*(3), 1591–1604. https://doi.org/10.1093/gji/ggaa065

Thrastarson, S., van Herwaarden, D.-P., & Fichtner, A. (2021). Inversionson: Fully automated seismic waveform inversions. *EarthArXiv*.

Thrastarson, S., van Herwaarden, D.-P., Krischer, L., Boehm, C., van Driel, M., Afanasiev, M., & Fichtner, A. (2022). Data-adaptive global full-waveform inversion. *Geophysical Journal International*, *230*(2), 1374–1393. https://doi.org/10.1093/gji/ggac122

Thrastarson, S., van Herwaarden, D.-P., Krischer, L., & Fichtner, A. (2021). LASIF: Large-scale seismic inversion framework, an updated version. *EarthArXiv*.

Thrastarson, S., van Herwaarden, D.-P., Noe, S., Schiller, C. J., & Fichtner, A. (2024a). The Long-wavelength Earth model (LOWE) at 50 s minimum period. *Zenodo*. https://doi.org/10.5281/ZENODO.11279695

Thrastarson, S., van Herwaarden, D.-P., Noe, S., Schiller, C. J., & Fichtner, A. (2024b). REVEAL: A global full-waveform inversion model. *Bulletin of the Seismological Society of America*, *114*(3), 1392–1406. https://doi.org/10.1785/0120230273

Trampert, J., Deschamps, F., Resovsky, J., & Yuen, D. (2004). Probabilistic tomography maps chemical heterogeneities throughout the lower mantle. *Science*, *306*(5697), 853–856. https://doi.org/10.1126/science.1101996

Tromp, J. (2020). Seismic wavefield imaging of Earth's interior across scales. *Nature Reviews Earth & Environment*, *1*(1), 40–53. https://doi.org/10.1038/s43017-019-0003-8

Vallée, M., & Douet, V. (2016). A new database of source time functions (STFs) extracted from the SCARDEC method. *Physics of the Earth and Planetary Interiors*, *257*, 149–157. https://doi.org/10.1016/j.pepi.2016.05.012

van Driel, M., Boehm, C., Krischer, L., & Afanasiev, M. (2020). Accelerating numerical wave propagation using wavefield adapted meshes. Part I: Forward and adjoint modelling. *Geophysical Journal International*, *221*(3), 1580–1590. https://doi.org/10.1093/gji/ggaa058

van Herwaarden, D.-P., Boehm, C., Afanasiev, M., Thrastarson, S., Krischer, L., Trampert, J., & Fichtner, A. (2020). Accelerated full-waveform inversion using dynamic mini-batches. *Geophysical Journal International*, *221*(2), 1427–1438. https://doi.org/10.1093/gji/ggaa079

van Herwaarden, D.-P., Thrastarson, S., Hapla, V., Afanasiev, M., Trampert, J., & Fichtner, A. (2023). Full-waveform tomography of the African plate using Dynamic Mini-Batches. *Journal of Geophysical Research: Solid Earth*, *128*(6), e2022JB026023. https://doi.org/10.1029/2022jb026023

Wang, X., & Zhan, Z. (2020a). Moving from 1-D to 3-D velocity model: Automated waveform-based earthquake moment tensor inversion in the Los Angeles region. *Geophysical Journal International*, *220*(1), 218–234. https://doi.org/10.1093/gji/ggz435

Wang, X., & Zhan, Z. (2020b). Seismotectonics and fault geometries of the 2019 Ridgecrest sequence: Insight from aftershock moment tensor catalog using 3-D Green's functions. *Journal of Geophysical Research: Solid Earth*, *125*(5), e2020JB019577. https://doi.org/10.1029/2020jb019577

Wehner, D., Blom, N., Rawlinson, N., Böhm, C., Miller, M. S., Supendi, P., & Widiyantoro, S. (2022). SASSY21: A 3-D seismic structural model of the lithosphere and underlying mantle beneath Southeast Asia from multi-scale adjoint waveform tomography. *Journal of Geophysical Research: Solid Earth*, *127*(3), e2021JB022930. https://doi.org/10.1029/2021jb022930

Wehner, D., Rawlinson, N., Greenfield, T., Daryono, Miller, M. S., Supendi, P., et al. (2022). SASSIER22: Full-waveform tomography of the Eastern Indonesian region that includes topography, bathymetry, and the fluid ocean. *Geochemistry, Geophysics, Geosystems*, *23*(11), e2022GC010563. https://doi.org/10.1029/2022gc010563

Wells, D. L., & Coppersmith, K. J. (1994). New empirical relationships among magnitude, rupture length, rupture width, rupture area, and surface displacement. *Bulletin of the Seismological Society of America*, *84*(4), 974–1002. https://doi.org/10.1785/bssa0840040974

Wuestefeld, A., Spica, Z. J., Aderhold, K., Huang, H.-H., Ma, K.-F., Lai, V. H., et al. (2023). The global DAS month of February 2023. *Seismological Research Letters*, *95*(3), 1569–1577. https://doi.org/10.1785/0220230180

Zhou, L., Zhang, W., Shen, Y., Chen, X., & Zhang, J. (2016). Location and moment tensor inversion of small earthquakes using 3D Green's functions in models with rugged topography: Application to the Longmenshan fault zone. *Earthquake Science*, *29*(3), 139–151. https://doi.org/10.1007/s11589-016-0156-1

Zhu, H., Bozdağ, E., & Tromp, J. (2015). Seismic structure of the European upper mantle based on adjoint tomography. *Geophysical Journal International*, *201*(1), 18–52. https://doi.org/10.1093/gji/ggu492

Zhu, L., & Zhou, X. (2016). Seismic moment tensor inversion using 3D velocity model and its application to the 2013 Lushan earthquake sequence. *Physics and Chemistry of the Earth, Parts A/B/C*, *95*, 10–18. https://doi.org/10.1016/j.pce.2016.01.002

References From the Supporting Information

Babuska, V., & Cara, M. (1991). *Seismic anisotropy in the Earth* (Vol. 10). Springer Science & Business Media.